Nanoscale

Nanoscale

PAPER

Preparation of hollow microsphere@onion-like solid nanosphere MoS$_2$ coated by carbon shell as stable anode for optimized lithium storage

Bangjun Guo, Ke Yu,[*] Haili Song, Honglin Li, Yinghua Tan, Hao Fu, Chao Li, Xiang Lei and Ziqiang Zhu

A one-step hydrothermal method was successfully used to fabricate hollow microsphere@onion-like solid nanosphere MoS$_2$. Then the as-prepared sS-MoS$_2$ was decorated with carbon shell which used dopamine as carbon source following a facile route, namely hollow microsphere@onion-like solid nanosphere MoS$_2$ decorated with carbon shell (sS-MoS$_2$@C). A synergistic effect was observed for the two-component material, leading to new electrochemical processes for lithium storage, with improved electroconductibility and structural soundness, triggering an ascending capacity upon cycling. The as-prepared sS-MoS$_2$@C exhibits optimized electrochemical behaviour with high specific capacity (1107 mA h g^{-1} at 100 mA g^{-1}), superior high-rate capability (805 mA h g^{-1} at 5000 mA g^{-1}) and good cycling stability (91.5% of capacity retained after 100 cycles), suggesting its potential application in high-energy lithium-ion batteries.

Introduction

Stimulated by the widespread usage of portable electronics and future electric vehicles, lithium-ion batteries (LIBs) have been regarded as high-efficiency and environmentally-friendly energy storage consumer electronics in our daily life.[1] With their applications extending into large-scale energy storage fields, such as power grids and transportation, traditional LIBs that are based on graphite electrode materials are limited by the intrinsically low theoretical capacities and cannot fulfill the increasing demand for energy storage. Therefore, there is an urgent need in the pursuit of high-capacity anode materials.[2] Developing high-performance electrode materials is one of the most effective approaches. For example, molybdenum disulfide (MoS$_2$), with a S-Mo-S sandwich layered structure analogous to graphite and a strong ability to host multiple Li ions, delivering a high theoretical specific capacity of 670 mA h g^{-1}.[3-5]

Sheet-like nanostructured MoS$_2$ and their composite material has been reported as one of the most promising LIBs anode material.[6-10] However, the practical application of sheet-like MoS$_2$ in LIBs has thus far been hindered by the concomitant substantial volume expansion, accompanying by the Li$^+$ ion insertion, generates mechanical strain that causes nanostructure pulverization and loss the integrity of active material, which further lead to the inefficient application of MoS$_2$ for Li storage.[11,12] To avoid this intrinsical trouble, designing a new firm structural nanomaterial is attainable. Compared with the sheet-like nanostructures, sphere nanostructures have been proved more structurally stable during the Li$^+$ ion insertion–extraction process in LIBs.[13-15] Since the sphere structure is the basic unit of nanomaterial, which could accommodate more

volume expansion and lower the mechanical strain during the Li$^+$ ion insertion, slowing down the crush of nanostructure. For application as LIBs anode material, the conversion reaction of MoS$_2$ during Li$^+$ ion discharge–charge process, results in the formation of metal Mo and Li$_2$S. Once Li$_2$S is formed, it becomes the active component, and its electrochemistry dominates in the subsequent cycles. While the Li$_2$S possess a low conductivity and poor cyclability, the capacity of MoS$_2$ anode material often fades quickly upon cycling.[9,16] Thus, without subsidiary protection, bare MoS$_2$ nanostructures cannot maintain their original morphology and high conductivity which resulting from the repeated lithiation–delithiation.[17] An efficient approach is known as nano-composite method, which aims to improve the structural stability through employing a second component such as carbon as the protective coating shell.[18] Benefiting from their large specific surface areas and porous architectures, covered nanocarbon shell serves two main functions: firstly, to buffer the volume variation of active MoS$_2$ and prevent the aggregation of pulverized active material; secondly, to protect the MoS$_2$ against direct contact with the electrolyte which may result in the formation of an unstable SEI film to lower the conductivity.[19,20] Recently, many efforts have been devoted to preparing MoS$_2$/carbon architectures assembled from nano-scaled building blocks. These architectures can effectively increase the electrolyte–electrode contact area, buffer the volume changes of electrodes and shorten the diffusion distance of ions.[21-23] Nonetheless, preparation of uniform hierarchical MoS$_2$ micro@nano sphere decorated with carbon shell for application in LIBs was rarely reported.

Based on this concept, we herein report the synthesis of a novel nanocomposite, in which hollow microsphere@onion-like solid nanosphere MoS$_2$ (sS-MoS$_2$) was synthesised by a facile one-step

hydrothermal method without any surfactant, and followed by a decoration of carbon shell which used dopamine as carbon source (sS-MoS$_2$@C). In serving as an anode material for LIBs, the sS-MoS$_2$ core acts as a host for Li storage, in which onion-like solid nanosphere MoS$_2$ principally provide an efficient storage for Li$^+$ ion and hollow microsphere MoS$_2$ primarily enhance the special surface area. Meanwhile, the carbon shell helps to protect the MoS$_2$ against direct contact with the electrolyte and promote a rapid charge-transfer reaction by providing an efficient electron pathway for the fast lithiation–delithiation. The cooperation of the two active components in sS-MoS$_2$@C brings about a favourable synergistic effect, leading to a higher capacity than that of the single components, resulting in an optimized cycling stability and outstanding rate behaviour for application as anode material of LIBs. The as-prepared material was also applied as anode material for coin cell which can easily power a light emitting diodes (LEDs).

Experimental

Synthesis of hollow microsphere@onion-like solid nanosphere MoS$_2$

Three-dimensional hollow microsphere@onion-like solid nanosphere MoS$_2$ was prepared under a one-step hydrothermal process. In a typical procedure, 0.2 g sodium molybdate and 0.4 g thioacetamide were dissolved in 60 mL deionized water in a beaker magnetic stirring for 10 min to obtain a transparent solution. Then 0.4 g oxalic acid were added into the above solution to adjust the pH value and the mixture was kept stirring for 30 min. The resulting uniform mixed solution was transferred into a 100 mL Teflon-lined stainless steel autoclave and hydrothermally treated at 200 °C for 24 h in an electric oven, then followed by natural cooling to room temperature. After cooling to room temperature, the as-prepared samples were washed extensively with deionized water several times and ultrasonication for 30 min to collect the black precipitate, and dried at 60 °C for 5 h in air.

Preparation of sS-MoS$_2$@C

The as-prepared sS-MoS$_2$ was decorated with carbon shell using dopamine as carbon source. Typically, 300 mg as-prepared sS-MoS$_2$ were dispersed in Tris-buffer (50 mL, 10 mM, pH = 8.5) by ultrasonication for 1 h to form a suspension. After that, 50 mg dopamine was added to the mixture under stirring. The mixture was subjected to continuous magnetic stirring at room temperature for 24 h. Afterwards, the precipitates, sS-MoS$_2$@poly-dopamine, were collected by centrifugation, then washed several times with deionized water, and then dried at 60 °C for 6 h. The obtained sS-MoS$_2$@poly-dopamine was then annealed at 800 °C for 5 h under Ar to convert the poly-dopamine into carbon. The obtained composite was named as sS-MoS$_2$@C-1. In order to tune the coating thickness of the carbon shell, sample sS-MoS$_2$@C-2 was prepared similarly to sS-MoS$_2$@C-1, but the initial concentration of dopamine was changed from 50 mg to 100 mg.

Characterizations

The morphology and structure of the samples were investigated by a field emission SEM (JEOL-JSM-6700F) operated at 15 kV and TEM (JEOL-2010) at 200 kV. TGA was carried out on a METTLER TOLEDO TGA/SDTA851e System under air flow. Surface area determination was performed by Brunauer–Emmett–Teller (BET). XRD patterns were collected on a Bruker D8 Advance diffractometer with Cu Kα radiation (λ=1.5418 Å). Raman spectral experiments were carried out by a Jobin-Yvon LabRAM HR 800 micro-Raman spectrometer. X-ray photoelectron spectra (XPS) were collected on a Kratos Axis ULTRA X-ray photoelectron spectrometer using a monochromatic Al Kα X-ray source and a hemispherical electron energy analyzer.

Electrochemical measurements

All the electrochemical tests were carried out in a two-electrode coin-cell (CR 2032) which assembled in an argon–filled glovebox (O$_2$ and H$_2$O levels < 0.1 ppm). The as-prepared sS-MoS$_2$@C and sS-MoS$_2$ were used as a working electrode, lithium foil as counter and reference electrodes, a polypropylene film (Celgard 2400) as a separator, and 1 mol L^{-1} LiPF$_6$ dissolved in a mixture of ethylene carbonate (EC) and dimethyl carbonate (DMC) (1 : 1 in volume) as an electrolyte. The working electrodes were prepared by a slurry tape casting procedure. The slurry consisted of 70 wt% active materials, 20 wt% carbon black and 10 wt% polyvinylidene fluoride (PVDF) dissolved in N-methyl-2-pyrrolidinone (NMP). The slurry was tape-cast on the copper foil, and dried under vacuum at 60 □ for 24 h and cut into circular pieces before use. Cyclic voltammetry (CV) profiles (0.01–3.0 V, 0.1 mV s^{-1}) were obtained on an electrochemical workstation (CHI 660D, Shanghai, China). Galvanostatic discharge–charge cycles of the cells were conducted between 0.01 and 3.00 V on a LAND CT-2001A battery cycler (Wuhan, China) at room temperature. Electrochemical impedance spectroscopy (EIS) was measured on the coin cell using an electrochemical workstation (Autolab PGSTAT302N, Netherlands) with amplitude of 0.5 mV over the frequency range from 200 kHz to 0.01 Hz.

Results and discussion

Schematic 1 illustrates the designed synthesis of hollow microsphere@onion-like solid nanosphere MoS$_2$ decorated with carbon shell. On the basis of our previous research, we reach a conclusion that two kinds of microsphere and nanosphere MoS$_2$ growth processes are simultaneous.[24] First, the formation mechanism of nanospheres is similar to the Ostwald ripening with a fast self-assembly nucleation and a slow evolution process. Second, the growth process of the microspheres was the growth of amorphous granules along with the spherical surfaces. Eventually, nanospheres and microspheres grow into well-dispersed structures.[25,26] We proposed a possible growth mechanism for sS-MoS$_2$ as below. At the very beginning of the heating process, numerous amorphous primary MoS$_2$ nanoparticles were formed in the Ⅰ stage. After heated to a certain temperature, these amorphous primary MoS$_2$ nanoparticles spontaneously aggregated into evacuating solid spheres, as shown in stage Ⅱ. In the Ⅲ stage, the loosened solid
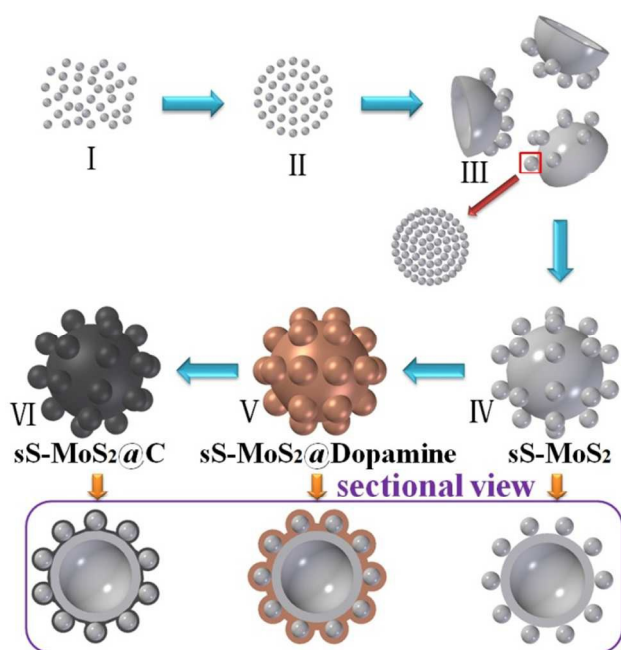
Scheme 1. Scheme for the fabrication of sS-MoS$_2$@C.

spheres finally crystallized into well layered onion-like structured nanospheres (Figure S1), meanwhile, the amorphous primary MoS$_2$ granules which are the source of the ultimate MoS$_2$ microspheres were initially formed at the temperature about 200 °C. These amorphous primary MoS$_2$ granules were generated during high temperature via the reaction of the remainder solute and in a stronger acidic reaction environment deriving from increasingly hydrolyze undecomposed oxalic acid. Because the factors of stronger acidic

solution, high temperature and low concentration these amorphous granules with different surface free energies aggregated into previous cambered pieces and grew along with the spherical surface, which resulted in the formation of hollow microspheres (stage IV). At the same time, nanospheres attached on the new cambered surfaces accompanying the growth of hollow MoS$_2$ microspheres. Usually, dopamine was equipped on the surface of sS-MoS$_2$ in the Tris-buffer solution. After overnight magnetic stirred and dried for 6 h, the sS-MoS$_2$@dopamine were collected (stage V).[27] Lastly, the sS-MoS$_2$@dopamine were annealed to get the sS-MoS$_2$@C at 800 °C under Ar atmosphere (stage VI).[28,29]

Scanning electron microscope (SEM) images are shown in Figure 1. According to Figure 1a, sS-MoS$_2$ has uniform microsphere@nanosphere morphology with a diameter distribution of about 2μm. As can be seen from the inset of Figure 1a, MoS$_2$ nanospheres distribute harmoniously on the surface of MoS$_2$ microsphere. Figure 1b shows the outside view of one single sS-MoS$_2$, the MoS$_2$ nanospheres are well-distributed on the shell with a diameter of 240−250 nm. The inset of Figure 1b displays an sS-MoS$_2$ with an obvious hole, which reveals the microsphere is hollow structure. The round arched structure as shown in Figure 1c, further proves the fact. Moreover, Figure 1c also shows the thickness of the microsphere shell ~80 nm. Generally, the sS-MoS$_2$@C inherits the morphology of the sS-MoS$_2$ (Figure 1d). While it is quite apparent that the surface of sS-MoS$_2$@C is not as smooth as the surface of pure sS-MoS$_2$. More details are shown in Figure 1e and the inset of Figure 1d. The morphology of sS-MoS$_2$@C-1 and sS-MoS$_2$@C-2 are demonstrated in Figure 1e and Figure 1f, respectively. Markedly, the carbon shell thickness of sS-MoS$_2$@C-2 is massive than that of sS-MoS$_2$@C-1, which may impede the electron beam penetrate into the inner sS-MoS$_2$ core.
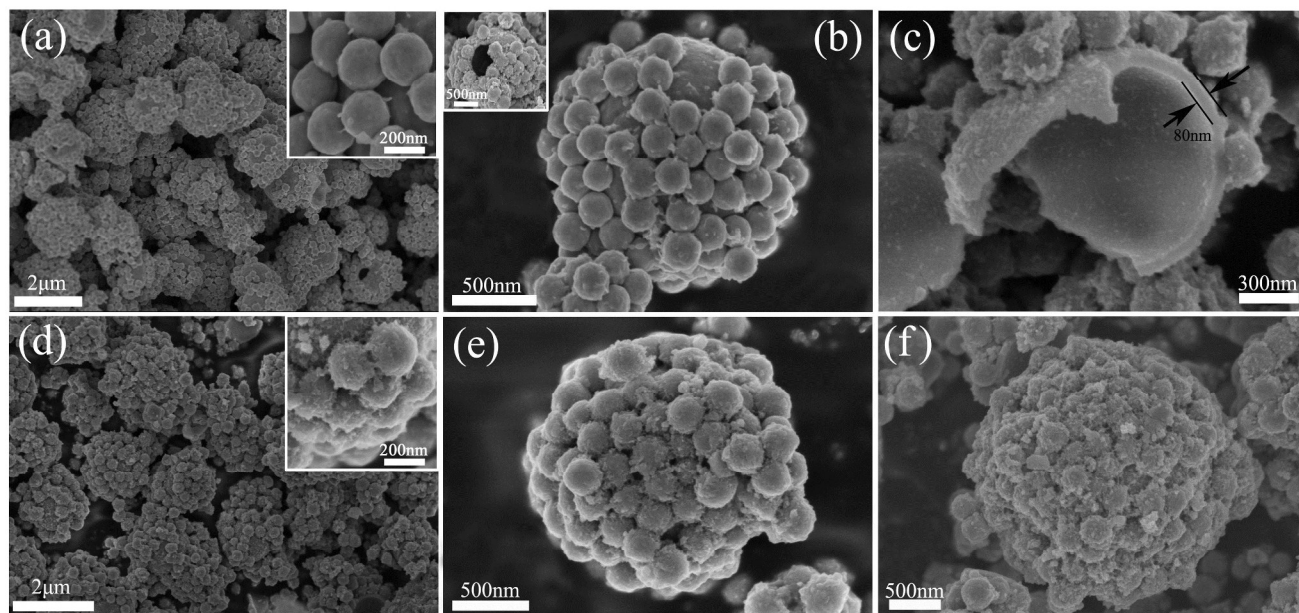

Figure 1. SEM images of bare sS-MoS$_2$ and sS-MoS$_2$@C. (a) Low magnification SEM image of sS-MoS$_2$ and the upper inset is the high magnification SEM image of sS-MoS$_2$. (b) Medium magnification SEM image of sS-MoS$_2$ and the upper inset is one broken sS-MoS$_2$. (c) Medium magnification SEM image of broken sS-MoS$_2$@C. (d) Low magnification SEM image of sS-MoS$_2$@C-1 and the upper inset is the high magnification SEM image of sS-MoS$_2$@C-1. (e) Medium magnification SEM image of sS-MoS$_2$@C-1. (f) Medium magnification SEM image of sS-MoS$_2$@C-2.
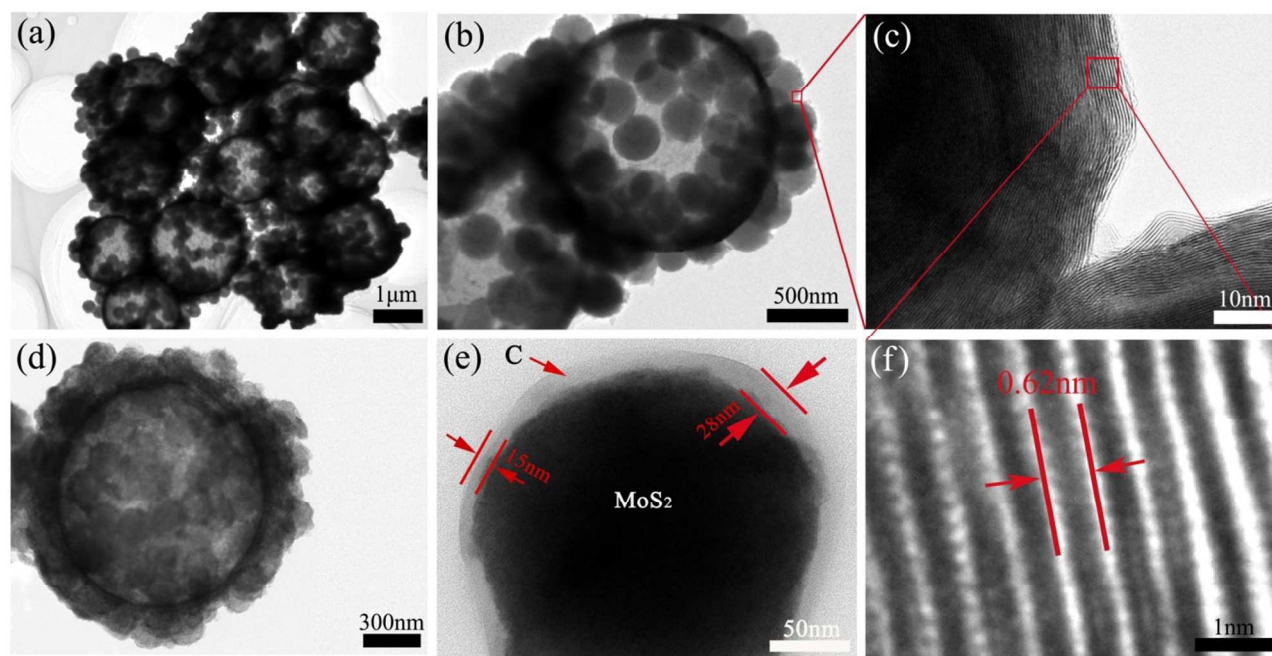
Figure 2. TEM images of bare sS-MoS$_2$ and sS-MoS$_2$@C. (a) Low magnification TEM image of sS-MoS$_2$. (b) Medium magnification TEM image sS-MoS$_2$. (c) High-resolution TEM image of onion-like solid nanosphere. (d) Medium magnification TEM image of sS-MoS$_2$@C-1. (e) High magnification TEM image of sS-MoS$_2$@C-1. (f) High-resolution TEM image of sS-MoS$_2$.

Transmission electron microscope (TEM) was further employed to investigate the internal structure of these composite materials. It is noticeable that almost every hollow microsphere is successfully and uniformly fabricated with MoS$_2$ nanospheres (Figure 2a), which can be put down to the assistant of oxalic acid and high temperature. Figure 2b displays one legible sS-MoS$_2$ structure, in which the surface of hollow microsphere and solid nanospheres are all smooth. Figure 2c is the HRTEM image of the rectangular area in Figure 2b. The striatures could be observed from the solid nanospheres MoS$_2$, which form the onion-like structure. From the high resolution TEM image (Figure 2f), it can be clearly distinguished that well-resolved interlayer distances with a spacing of 0.62 nm, which corresponds to the (002) plan of MoS$_2$. After dopamine cladding and high temperature annealing treatment, the outer spheres of MoS$_2$ are almost covered with carbon shells (Figure 2d). The composite structure was further confirmed by HRTEM. As shown in Figure 2e, superficial nanosphere is encapsulated by a self-supporting carbon shell with a uniform thickness of 15−30 nm. The MoS$_2$ core is closely attached to the outside carbon shell, the direct facet-to-facet contact of the MoS$_2$ core and conductive carbon shell makes the core more accessible to both Li$^+$ ion and electron.

The crystalline structure of the obtained materials was investigated by X-ray diffraction (XRD) (Figure 3a). The majority of the diffraction peaks, especially for those with high intensity, can be assigned to the crystalline planes of hexagonal MoS$_2$ phase (JCPDS card No. 37–1492). Especially, the distinct peak at 14.2° characteristic of the (002) crystalline plane for MoS$_2$ suggests the ordered stacking of S-Mo-S layers,[30,31] which is in good agreement with the TEM image observed in Figure 2f. The XRD pattern for the sS-MoS$_2$@C-1 and sS-MoS$_2$@C-2 are respectively shown as the curve (I) and curve (II), no diffraction peaks from graphitic carbon

can be detected, indicating the amorphous nature of the carbon shell.[18] The disappeared peaks of (103) and (105) for sS-MoS$_2$@C could be attributed to the surface strain, induced by the coated carbon shell on the MoS$_2$ spheres surface. Moreover, the broad peak emerges at 60° is evolved from peak of (100), which could be explained as the variation of partial grain size from sS-MoS$_2$@C to sS-MoS$_2$. Thirdly, the XRD spectrum shows the crystal structure of compounds. The crystallinity of sS-MoS$_2$ might be decreased, during the carbon coated progress and annealing treatment, which brings about these differences from pristine sS-MoS$_2$. Raman spectroscopy was further utilized to characterize the composition of the obtained sS-MoS$_2$, sS-MoS$_2$@C-1 and sS-MoS$_2$@C-2. As shown in Figure 3b, all three materials was observed two distinct peaks at the bands of 380 and 407 cm^{-1}, which correspond to E$^1_{2g}$ vibration mode (the in-layer displacement of Mo and S atoms) and A$_{1g}$ vibration mode (the out-of-layer symmetric displacements of S atoms along the c axis).[32-34] In addition, another two markedly peaks at the bands of 1357 and 1572 cm^{-1} were also observed in sS-MoS$_2$@C-1 and sS-MoS$_2$@C-2, which can be severally assigned to the sp^3-hybridized disordered carbon (D-band) and the sp^2-hybridized graphitic carbon (G-band).[33,34] Moreover, the relative intensity of I$_D$ and I$_G$ (I$_D$: I$_G$≈ 0.95) suggests that the quantity of amorphous carbon is almost as many as the quantity of graphitic carbon.

Thermo gravimetric analysis (TGA) analysis was carried out to determine the carbon content of sS-MoS$_2$@C (Figure 3c). On one hand, for the origin sS-MoS$_2$ micro@nano structure, a weight loss (about 8.95%) at approximately 400 °C owing to the oxidative reaction of MoS$_2$ to MoO$_3$ under air atmosphere.[6,23] On the other hand, for the sS-MoS$_2$@C the main weight loss between 300 °C and 450 °C can be attributed to the combustion of carbon in air. For the composite materials, weight losses are respective 21.75% and
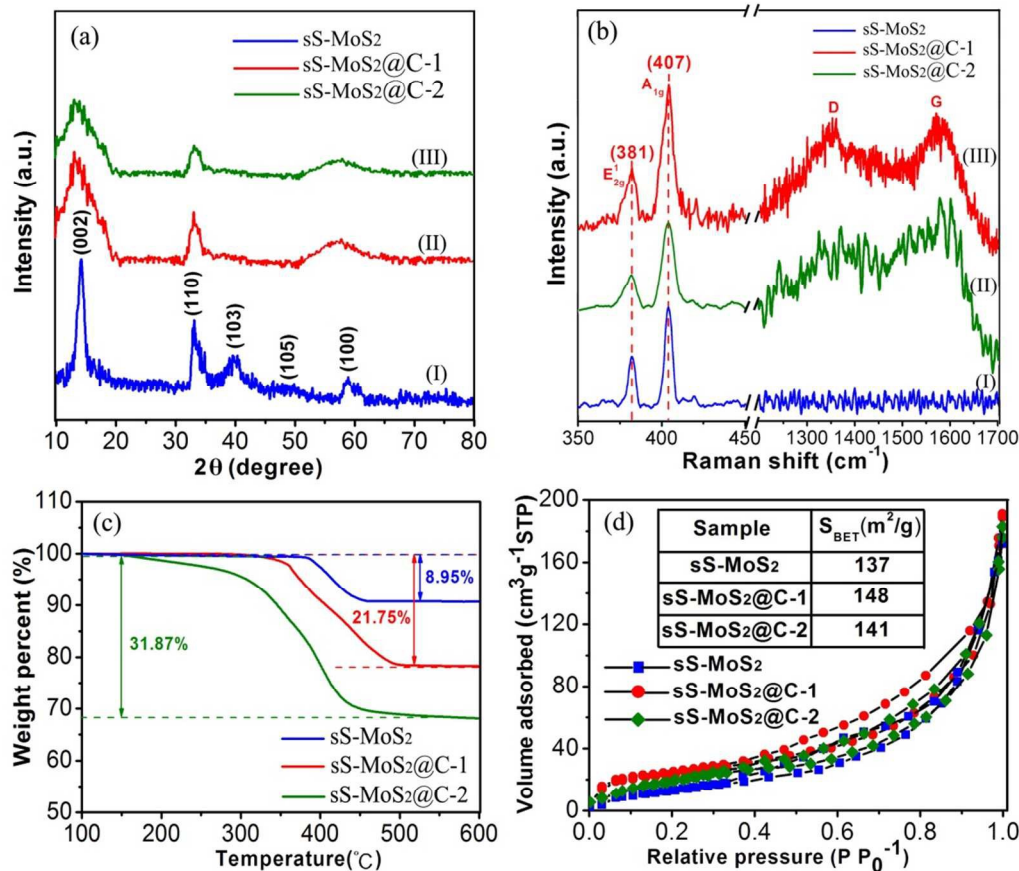
Figure 3. (a) XRD patterns and (b) Raman spectra of bare sS-MoS$_2$, sS-MoS$_2$@C-1 and sS-MoS$_2$@C-2 composites. (c) TG curves of sS-MoS$_2$, sS-MoS$_2$@C-1 and sS-MoS$_2$@C-2 under air atmosphere. (d) N$_2$ adsorption–desorption isotherms of sS-MoS$_2$, sS-MoS$_2$@C-1 and sS-MoS$_2$@C-2.

31.87%, corresponding to the content of carbon in sS-MoS$_2$@C-1 and sS-MoS$_2$@C-2 composites are 12.8% and 22.92%. To study the porous micro@nano structure of sS-MoS$_2$ and sS-MoS$_2$@C, N$_2$ adsorption–desorption isotherms were carried out. It can be seen from Figure 3d that the Brunauer-Emmett-Teller (BET) surface area of sS-MoS$_2$@C-1 is calculated to be 148 m^2 g^{-1} with a slight improvement as compared with that of sS-MoS$_2$ (137 m^2 g^{-1}) and sS-MoS$_2$@C-2 (141 m^2 g^{-1}). Such a high surface area of sS-MoS$_2$@C-1

nanostructure could be attributed to following reasons. Firstly, the hollow MoS$_2$ microsphere provides large interspaces which contribute mainly to the improvement of surface area. Secondly, amorphous carbon shell also enhances the outer surface area.

In order to confirm the existence and explore the distribution of the carbon shell in the as-formed sS-MoS$_2$@C-1 nanomaterial, energy dispersive X-ray (EDX) mapping analysis and scanning transmission electron microscopy (STEM) were carried out in Figure 4. Mapping analyses on a typical
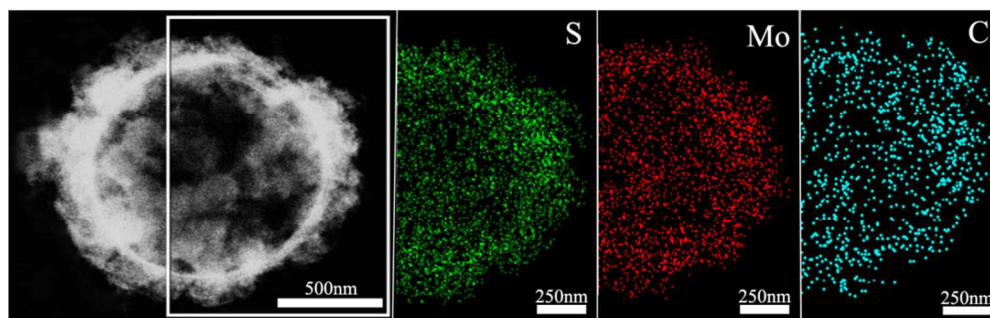

Figure 4. Scanning transmission electron microscopy (STEM) image of sS-MoS$_2$@C microstructure, and the EDX mapping images of S, Mo and C elements.
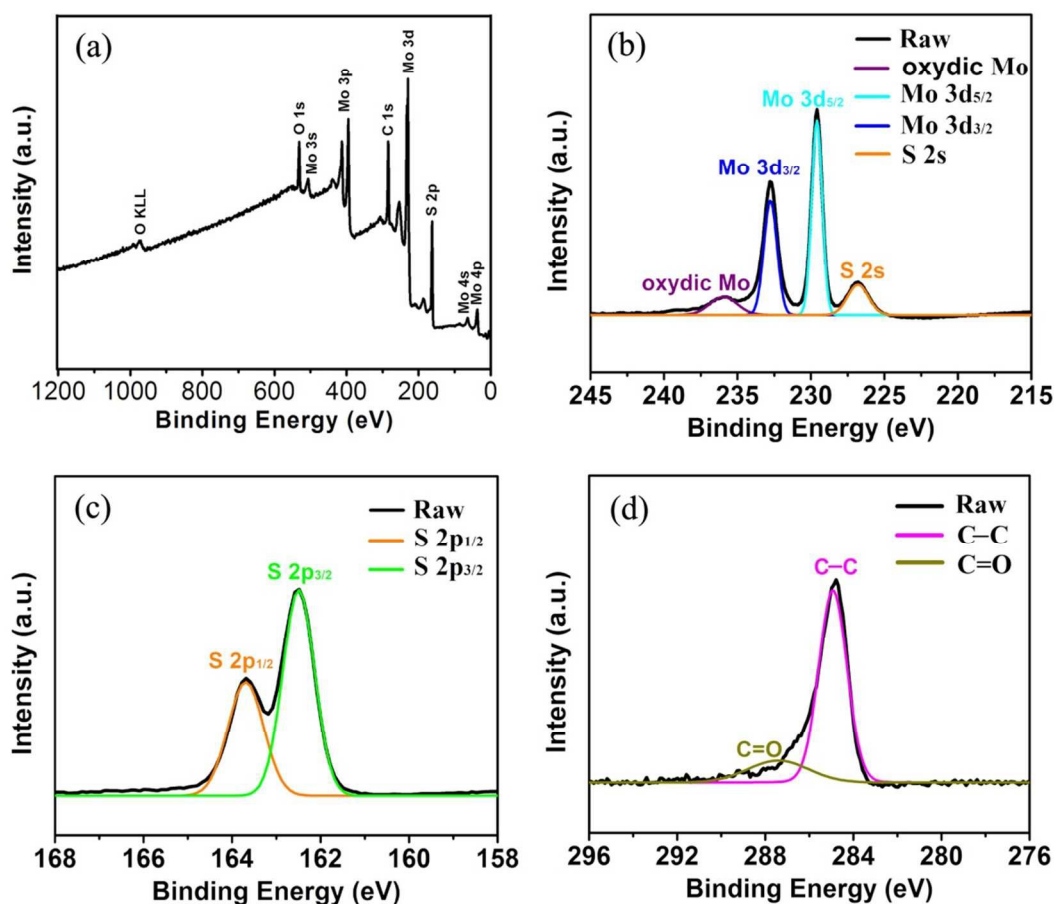
Figure 5. XPS spectra of sS-MoS₂@C-1 (a) Survey spectrum. (b) Mo 3d spectrum. (c) S 2p spectrum. (d) C 1s spectrum.

microsphere@nanosphere MoS₂ decorated with carbon shell reveals the presence of elements not only Mo and S but also C. A core-shell structure of sS-MoS₂@C-1 is remarkably manifested with a slightly larger circle area of C as compared with that of Mo and S, which proves the existence of carbon shell on the surface of sS-MoS₂. To further characterize the bonding state and chemical nature of the as-prepared sS-MoS₂@C nanocomposites, X-ray photoelectron spectroscopy (XPS) was employed. As can be seen from Figure 5a, the peaks of C, O, S and Mo can be obviously detected. Figure 5b shows the high-resolution spectrum of Mo 3d, two peaks are located at 229.5 eV and 232.7 eV, which are attributed to the Mo^{4+} $3d_{5/2}$ and Mo^{4+} $3d_{3/2}$, respectively.[35,36] A small S 2s peak is also observed which is located at 226.7 eV, and peak of oxydic Mo observed at 235.9 eV. In the peaks of S 2p (Figure 5c), the peaks at about 162.5 eV and 163.6 eV are related to the S $2p_{3/2}$ and S $2p_{1/2}$ binding energies, respectively. These surveyed spectrums are in good agreement with the previous studies which can be assigned to the characteristic of MoS₂.[37-39] Figure 5d shows the binding energy of C 1s at 284.8 eV which is attributed to the amorphous carbon (C–C bond) and peak of 287.2 eV have assigned to C=O bond. The XPS spectrum also demonstrates the carbon shell covered structure of sS-MoS₂@C

composites, which providing a prediction of better conductibility for using as anode materials of LIBs.

To understand the Li^+ storage properties of the sS-MoS₂@C-1 nanocomposites, the initial five cyclic voltammetry (CV) has been examined as shown in Figure 6a. During the first cathodic process, a reduction peak appears at approximately 0.85 V corresponding to the phase transition from trigonal prismatic to octahedral coordination. The second cathodic peak at about 0.32 V corresponds to the subsequent conversion reaction to form Mo nanoparticles embedded in Li₂S, and then the formation of a gel-like polymeric layer resulting from electrochemically driven electrolyte degradation.[40,41] In the reverse scan, a ambiguous anodic peak at 1.75 V is due to the incomplete oxidation of Mo metal, and another pronounced peak at 2.38 V can be put down to the delithiation of Li₂S.[42,43] In the remainder scans, the intensities of the two cathodic peaks at about 0.85 V and 0.32 V are disappeared drastically. Meanwhile, two new peaks at 1.05 V and 1.82 V are observed, which indicates the multistep conversion process from S to the formation of Li₂S. The cathodic peak at 1.82 V and anodic peak at 2.38 V constitute a reversible redox couple, which is the main electrochemistry process of this electrode.[44] It is also noted that a weak redox couple of cathodic peak at 0.25 V and
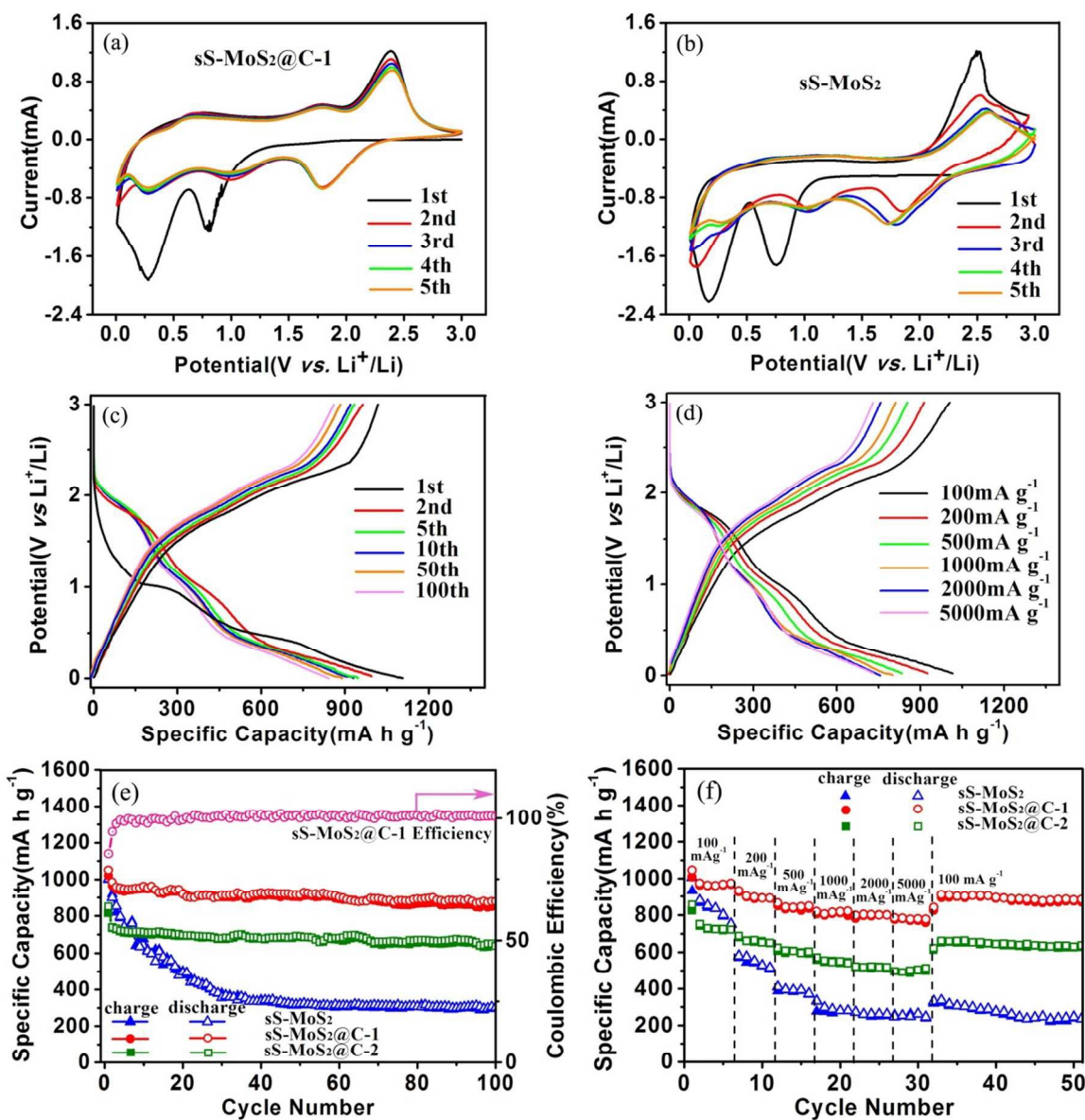
Figure 6. The initial five CV curves of (a) sS-MoS$_2$@C-1 and (b) sS-MoS$_2$ electrodes. (c) Discharge–charge voltage profiles at current density of 100 mA g^{-1} of sS-MoS$_2$@C-1. (d) Discharge–charge voltage profiles of sS-MoS$_2$@C-1 at different current densities. (e) Comparative long-term cycling performances of sS-MoS$_2$, sS-MoS$_2$@C-1 and sS-MoS$_2$@C-2 at current density of 100 mA g^{-1}. (f) Comparative rate performance of sS-MoS$_2$, sS-MoS$_2$@C-1 and sS-MoS$_2$@C-2 at different current densities.

anodic peak at 0.5 V was observed, which could be accounted for the auxiliary action of electrochemical Li$^+$ storage by amorphous carbon shell.[34,45] Therefore, it is clear that the carbon shell do assist in electrochemical reaction during discharge–charge. After the first cycle, the electrochemical performance of sS-MoS$_2$@C-1 is mainly dominated by the reversible conversion reaction of sulfur to Li$_2$S. As can be seen from the Figure 6a, the CV performance is very stable and steady, indicating the sS-MoS$_2$@C-1 composite materials have a high reversibility and good stability for the insertion-desertion of Li$^+$. For the bare sS-MoS$_2$ electrode, two redox peaks located at 0.21/0.78 V and 2.48 V in the first cycle correspond to the conversion reaction process: MoS$_2$ + 4Li$^+$ + 4e$^-$↔Mo + 2Li$_2$S,

which agrees well with the previous lithiation and delithiation profiles of sS-MoS$_2$@C-1 composites. While in the subsequent cycles, the intensity of anodic peak changed greatly, suggesting an irreversible conversion reaction during the Li$^+$ insertion–extraction process. It is also worthy to be mentioned that the shape of the peaks for the sS-MoS$_2$@C-1 nanocomposites is more intense and sharper, and the gap between redox peaks is smaller than that for the sS-MoS$_2$, demonstrating that the sS-MoS$_2$@C-1 had a greater efficiency of the redox reaction and lower overall resistance.[7,46] These CV behaviours also demonstrate that sS-MoS$_2$@C-1 possess a much better stability than sS-MoS$_2$ for application as anode materials of LIBs.

Figure 6c shows the galvanostatic discharge–charge (GDC)

voltage profiles of sS-MoS$_2$@C-1 nanocomposites at 100 mA g^{-1}. During the first discharge, two plateaus appear at approximately 1.0 V and 0.5 V, corresponding to the phase transformation and further decomposition into Li$_2$S and Mo nanoparticles, respectively.[16,17] The first discharge process should be associated with the Li$^+$ insertion reaction followed by a conversion reaction. The sloped profile at <0.5 V suggests interfacial Li uptake by the carbon shell.[47] In the subsequent charge, the distinct plateau at 2.3 V agrees well with the anodic peak during CV scan, which is attributed to the oxidation of Li$_2$S.[48,49] The subsequent GDC cycles show sloped profiles, with two plateaus at approximately 1.85 V and 2.3 V upon discharge–charge, corresponding to the conversion reaction of sulfur to Li$_2$S. In the first cycle, the discharge and charge capacities of sS-MoS$_2$@C-1 are respectively 1107 mA h g^{-1} and 1008 mA h g^{-1}, with a Coulomb Efficiency (CE) of 91%. Moreover, the reversible discharge–charge capacities of the 2nd and 5th cycles are respectively 995–953 mA h g^{-1} and 947–933 mA h g^{-1}. As the initial irreversible capacity loss is mainly attributed to the formation of SEI, the CE improvement is largely due to the carbon shell, which inhibits the side reactions of sS-MoS$_2$ by diminishing their unfavourable contact with the electrolyte. After several cycles, the Coulomb Efficiency quickly approaches to 100%, with 10th, 50th, 100th discharge–charge capacities of 930–921 mA h g^{-1}, 896–891 mA h g^{-1} and 889–886 mA h g^{-1}, respectively. The sS-MoS$_2$@C-1 nanocomposite also exhibits improved cycling and rate performance, as shown in Figure 6d. Even at high current density of 1000 mA g^{-1}, 2000 mA g^{-1} and 5000 mA g^{-1}, the GDC voltage profiles of sS-MoS$_2$@C-1 remains high and stably, with reversible discharge–charge capacities of 825–819 mA h g^{-1}, 811–805 mA h g^{-1} and 796–791 mA h g^{-1}, respectively.

The cyclic stability and coulombic efficiency of the bare sS-MoS$_2$, sS-MoS$_2$@C-1 and sS-MoS$_2$@C-2 nanocomposites at a current density of 100 mA g^{-1} are presented in Figure 6e. It is evidenced that sS-MoS$_2$@C-1 outperforms the other two samples in cycling stability. The almost completely stable cycling performance of sS-MoS$_2$@C-1 starts from the third cycle. The discharge capacity of sS-MoS$_2$@C-1 composites stabilizes at about 960 mA h g^{-1} after three cycles. Even after 100 cycles, a high capacity of 878 mA h g^{-1} can be maintained, which is 91.5% of the capacity at the third cycle. It is also could be seen from the Figure 6e that the Coulomb Efficiency maintained a high level at about 100% from the third cycle onwards. In sharp contrast, sS-MoS$_2$ shows a much inferior cycling performance. Although it delivers a high initial discharge capacity (998 mA h g^{-1}), the capacity of bare sS-MoS$_2$ prepared in this work decreases continuously within 20 cycles. After 100 cycles, a low capacity of 302 mA h g^{-1} is remained. The cycling stability for sS-MoS$_2$@C-2 is somewhat better than that of sS-MoS$_2$, but still inferior to that of sS-MoS$_2$@C-1. The initial discharge capacity is 830 mA h g^{-1}, and the capacity fades to 638 mA h g^{-1} after 100 cycles. Compared with the high capacity of sS-MoS$_2$@C-1, the relative lower capacity of sS-MoS$_2$@C-2 could be attributed to the too thick carbon shell impeding the high-efficiency transport of Li$^+$. The rate performance of sS-MoS$_2$, sS-MoS$_2$@C-1 and sS-MoS$_2$@C-

2 nanocomposites were further investigated by cycling at various discharge–charge current densities ranging from 100–5000 mA g^{-1} (Figure 6f). sS-MoS$_2$@C-1 delivers a high capacity of 980 mA h g^{-1} at 100 mA g^{-1}. As the current density gradually elevates, the capacity decreases slightly. Even at a high current density of 5000 mA g^{-1}, 805 mA h g^{-1} of discharge capacity can still be retained, suggesting the excellent high rate capability of sS-MoS$_2$@C-1 nanocomposites. Remarkably, a stable capacity of 910 mA h g^{-1} can be attained when the current is reduced to 100 mA g^{-1}. The electrochemical performance of sS-MoS$_2$@C-2 in terms of cycling stability and rate capability is comparable or even superior to those of MoS$_2$ based anodes in previous reports,[6,7,23,40] with a high capacity of 526 mA h g^{-1} at 5000 mA g^{-1}, suggesting the effectiveness of our strategy in introducing the carbon shell. On the contrary, the bare sS-MoS$_2$ deliver much lower capacities at high current densities, and fails quickly for the 20th cycle at 1000 mA g^{-1}. It is obvious that the capacity of bare sS-MoS$_2$ fades rapidly and cannot recover to the initial level even at 100 mA g^{-1} after high rate cycling. Considering that all samples have almost the same sS-MoS$_2$ core structure, the difference in capacity should be contributed from the carbon shell. First, the micro@nano spherical structure of MoS$_2$ core plays the role of buffering the mechanical stresses induced by the volumetric expansion–shrinkage and preventing the aggregation of MoS$_2$
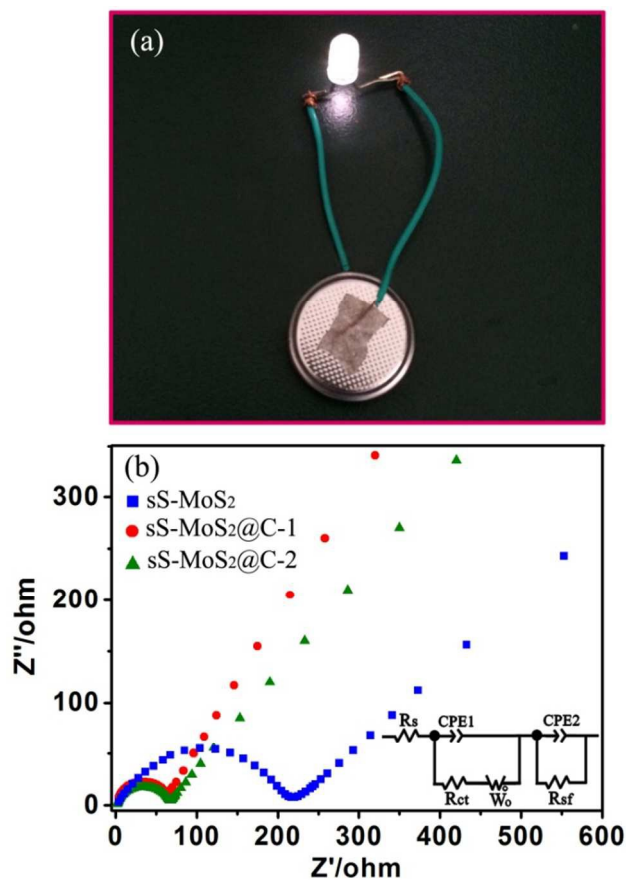

Figure 7. (a) Photograph of a LEDs powered by one coin cell based on the sS-MoS2@C-1 electrode. (b) Nyquist plots of the sS-MoS$_2$, sS-MoS$_2$@C-1 and sS-MoS$_2$@C-2 electrodes in the frequency range from 200 kHz to 0.01 kHz.

cathode material. Second, the carbon shell may serve as shields and adsorbents to restrain the discharge products of sulfur from dissolving into electrolytes. These results show that only with the optimal molar ration of MoS_2 to carbon, the composites can exhibit enhanced Li^+ storage properties.

Such high capacity retention of the sS-MoS_2@C-1 electrode accounts for its structural stability. To demonstrate the applications, we show that one coin cell based on the sS-MoS_2@C-1 positive electrode, after being cycled 100 times at 100 mA g^{-1}, can still easily power a LEDs (3V, 20mA), as shown in Figure 7a. For a better understanding of the unique sS-MoS_2@C architectures possesses such excellent electrochemical performances for lithium storage, we performed electrochemical impedance spectroscopy (EIS) for these three electrodes as shown in Figure 7b. It can be obviously seen that, the diameter of the semicircle for sS-MoS_2@C-1 in the high–medium frequency region is the smallest to those of sS-MoS_2 and sS-MoS_2@C-2, which demonstrates that sS-MoS_2@C-1 possess the lowest contact and charge-transfer resistances. The kinetic differences of these electrodes were further investigated using the common R-C equivalent circuit, as shown in the inset of Figure 7b. The inclined line in the low frequency region is descriptive of the Li^+ diffusion impedance, the medium frequency semicircle to the charge transfer resistance R_{ct} and CPE2 of the electrode–electrolyte interface, and the high frequency semicircle could be attributed to resistance R_{sf} and CPE1 of the SEI film.[40,50] The R_{ct} was obtained by fitting data according to the equivalent circuit model that sS-MoS_2, sS-MoS_2@C-1 and sS-MoS_2@C-2 electrodes have a charge transfer resistance of 225 Ω, 58 Ω and 75 Ω, respectively. These results clearly validates that the hollow microsphere@onion-like solid nanosphere MoS_2 decorated with carbon shell architecture can not only ensure a high conductivity of the overall electrode, but also largely enhance the electrochemical activity of sS-MoS_2 anode materials during cycle processes. The deliberately designed hollow microsphere@onion-like solid nanosphere MoS_2 decorated with carbon shell confirms that it can achieve excellent cycling performance as well as high capacity and superior rate capability, which could be explained as follows. Firstly, the onion-like MoS_2 nanosphere distributed on the surface of hollow MoS_2 microsphere with well arranged layer structure could availably buffering the mechanical stresses induced by the volumetric expansion–shrinkage, and the uniform spherical structure could prevent the aggregation of MoS_2 layers in molecular structure topology theory. Secondly, the sS-MoS_2 core acts as a host for Li storage, in which onion-like solid nanosphere MoS_2 principally provide an efficient storage for Li^+ ion and hollow microsphere MoS_2 primarily enhance the special surface area. Thirdly, the carbon shell not only enables fast e^- transmission, but also provides an unperturbed Li^+ supply for the core micro@nano MoS_2 spheres, which improving the Li storage kinetics and the stability of the composites. Lastly, the built carbon shell acts as shields to stabilize the sS-MoS_2 core structure and against the direct contact with the electrolyte to restrain the active material from dissolving. Thus, all the structural advantages of sS-MoS_2@C and the synergistic effect of sS-MoS_2 and carbon shell contribute to the stable cycling performance and excellent battery capacity.

Conclusions

In summary, hollow microsphere@onion-like solid nanosphere MoS_2 decorated with carbon shell structure was prepared, utilizing dopamine as carbon source. The successfully prepared core-shell sS-MoS_2@C nanocomposites have been engineered to fit the volume expansion during lithiation and enlarge the electric conductivity served as the electrode material. In addition to molybdenum disulfide, our concept of preparation the micro@nano sphere material can also be applied to other transition metal dichaldogenides (TMDs) materials, such as WS_2, $MoSe_2$ and TaS_2. With an optimized thickness of carbon shell, the sample sS-MoS_2@C-1 exhibits high reversible capacity, superior rate performances and excellent cycling stability. Furthermore, this work provides an insight that spherical MoS_2 nanostructures covered by carbon shell could be made for promising high-energy LIBs anode materials.

Acknowledgements

Notes and references

Key Laboratory of Polar Materials and Devices (Ministry of Education of China), Department of Electronic Engineering, East China Normal University, Shanghai, 200241, P. R. China. Fax: +86-21-54345198; Tel: +86-21-54345198; E-mail: yk5188@263.net

1 M. Armand and J. M. Tarascon, Nature, 2008, 451, 652–657.

2 K. Kang, Y. S. Meng, J. Breger, C. P. Grey and G. Ceder, Science, 2006, 311, 977–980.

3 H. Liu, D. Su, R. Zhou, B. Sun, G. Wang and S. Z. Qiao, Adv. Energy Mater., 2012, 2, 970–975.

4 T. Stephenson, Z. Li, B. Olsen and D. Mitlin, Energy Environ. Sci., 2014, 7, 209–231.

5 X. Cao, Y. Shi, W. Shi, X. Rui, Q. Yan, J. Kong and H. Zhang, Small, 2013, 9, 3433–3438.

6 F. Zhou, S. Xin, H. W. Liang, L. T. Song and S. H. Yu, Angew. Chem. Int. Ed., 2014, 53, 11552–11556.

7 S. Hu, W. Chen, J. Zhou, F. Yin, E. Uchaker, Q. F. Zhang and G. Z. Cao, J. Mater. Chem. A, 2014, 2, 7862–7872.

8 U. K. Sen and S. Mitra, ACS Appl. Mater. Interfaces, 2013, 5, 1240–1247.

9 L. C. Yang, S. N. Wang, J. J. Mao, J. W. Deng, Q. S. Gao, Y. Tang and O. G. Schmidt, Adv. Mater., 2013, 25, 1180–1184.

10 L. R. Hu, Y. M. Ren, H. X. Yang and Q. Xu, ACS Appl. Mater. Interfaces, 2014, 6, 14644–14652.

11 S. Ding, J. S. Chen and X. W. Lou, Chem. Eur. J., 2011 17, 13142–13145.

12 G. Huang, T. Chen, W. Chen, Z. Wang, K. Chang, L. Ma, F. Huang, D. Chen and J. Y. Lee, Small, 2013, 9, 3693–3703.

Nanoscale Accepted Manuscript

13 S. J. Ding, J. S. Chen, Z. Y Wang, Y. L. Cheah, S. Madhavi, X. Hu and X. W. Lou, J. Mater. Chem., 2011, 21, 1677–1680.

14 L. C. Liu, Q. Fan, C. Z. Sun, X. R. Gu, H. Li, F. Gao, Y. F. Chen and L. Dong, J. Power Sources, 2013, 221, 141–148.

15 S. J. Ding, D. Y. Zhang, J. S. Chen and X. W. Lou, Nanoscale, 2012, 4, 95–98.

16 K. Chang and W. Chen, ACS Nano, 2011, 5, 4720–4728.

17 Y. G. Li, H. L.Wang, L. Xie, Y. Y. Liang, G. S. Hong and H. J. Dai, J. Am. Chem. Soc., 2011, 133, 7296–7299.

18 H. W. Zhang, L. Zhou, O. Noonan, D. J. Martin, A. K. Whittaker and C. Z. Yu, Adv. Funct. Mater., 2014, 24, 4337–4342.

19 X. W. Lou, C. M. Li and L. A. Archer, Adv. Mater., 2009, 21, 2536–2539.

20 J. M. Jeong, B. G. Choi, S. C. Lee, K. G. Lee, Y. B. L. Chang, H. U. Lee, S. Kwon, G. Lee, C. S. Lee and Y. S. Huh, Adv. Mater., 2013, 25, 6250–6255.

21 J. J. Wang, C. Luo, T. Gao, A. Langrock, A. C. Mignerey and C. S. Wang, Small, 2015, 4, 472–480.

22 J. M. Jeong, K. G. Lee, S. J. Chang, J. W. Kim, Y. K. Han, S. J. Leea and B. G. Choi, Nanoscale, 2015, 7, 324–329.

23 Z. M. Wan, J. Shao, J. J. Yun, H. Y. Zheng, T. Gao, M. Shen, Q. T. Qu and H. H. Zheng, Small, 2014, 23, 4975–4981.

24 Y. H. Tan, K. Yu, T. Yang, Q. F. Zhang, W. T. Cong, H. H. Yin, Z. L. Zhang, Y. W. Chen and Z. Q. Zhu, J. Mater. Chem. C, 2014, 2, 5422–5430.

25 H. C. Zeng, Curr. Nanosci., 2007, 3, 177–181.

26 H. Shi, K. Yu, F. Sun and Z. Q. Zhu, CrystEngComm, 2012, 14, 278–285.

27 R. Liu, S. M. Mahurin, C. Li, R. R. Unocic, J. C. Idrobo, H. J. Gao, S. J. Pennycook and S. Dai, Angew. Chem. Int. Ed., 2011, 50, 6799–6802.

28 C. Lei, F. Han, D. Li,W. C. Li, Q. Sun, X. Q. Zhang and A. H. Lu, Nanoscale, 2013, 5, 1168–1175.

29 H. S. Li, L. F. Shen, K. B. Yin, J. Ji, J. Wang, X. Y. Wang and X. G. Zhang, J. Mater. Chem. A, 2013, 1, 7270–7276.

30 H. Li, Z. X. Wang, L. Q. Chen and X. J. Huang, Adv. Mater., 2009, 21, 4593–4607.

31 J. S. Chen and X. W. Lou, J. Power Sources, 2010, 195, 2905–2908.

32 Y. Shi, Y. Wang, J. I. Wong, A. Y. S. Tan, C. L. Hsu, L. J. Li, Y. C. Lu and H. Y. Yang, Sci. Rep., 2013, 3, 2169–2176.

33 X. Zhao, C. Hu and M. Cao, Chem. Asian J., 2013, 8, 2701–2707.

34 Z. Wang, T. Chen, W. Chen, K. Chang, L. Ma, G. Huang and D. Chen, J. Y. Lee, J. Mater. Chem. A, 2013, 1, 2202–2210.

35 J. Zheng, H. Zhang, S. Dong, Y. Liu, C. T. Nai, H. S. Shin, H. Y. Jeong, B. Liu and K. P. Loh, Nat. Commun., 2013, 5, 2995–2999.

36 D. H. Youn, J. W. Jang, J. Y. Kim, J. S. Jang, S. H. Choi and J. S. Lee, Sci. Rep., 2014, 4, 5492–5499.

37 K. K. Liu, W. Zhang, Y. H. Lee, Y. C. Lin, M. T. Chang, C. Y. Su, C. S. Chang, H. Li, Y. Shi and H. Zhang, Nano Lett., 2012, 12, 1538–1544.

38 C. Altavilla, M. Sarno and P. Ciambelli, Chem. Mater., 2011, 23, 3879–3885.

39 X. L. Li and Y. D. Li, J. Phys. Chem. B, 2004, 108, 13893–13900.

40 B. J. Guo, K. Yu, H. Fu, Q. Q. Hua, R. J. Qi, H. L. Li, H. L. Song, S. Guo and Z. Q. Zhu, J. Mater. Chem. A, 2015, 3, 6392–6402.

41 Q. Wang and J. Li, J. Phys. Chem. C, 2007, 111, 1675–1682.

42 Y. Gong, S. Yang, L. Zhan, L. Ma, R. Vajtai and P. M. Ajayan, Adv. Funct. Mater., 2014, 24, 125–130.

43 K. Zhang, H. J. Kim, X. Shi, J. T. Lee, J. M. Choi, M. S. Song and J. H. Park, Inorg. Chem., 2013, 52, 9807–9812.

44 G. He, S. Evers, X. Liang, M. Cuisinier, A. Garsuch and L. F. Nazar, ACS Nano, 2013, 7, 10920–10930.

45 E. Benavente, M. Santa Ana, F. Mendizabal and G. Gonz´alez, Coord. Chem. Rev., 2002, 224, 87–109.

46 L. Shen, E. Uchaker, X. Zhang and G. Cao, Adv. Mater., 2012, 24, 6502–6506.

47 J. R. Dahn, T. Zheng, Y. Liu and J. S. Xue, Science, 1995, 270, 590–593.

48 Y. X. Yin, S. Xin, Y. G. Guo and L. J.Wan, Angew. Chem. Int. Ed., 2013, 52, 13186–13200.

49 X. P. Fang, C. X. Hua, X. W. Guo, Y. S. Hu, Z. X. Wang, X. P. Gao, F. Wu, J. Z. Wang and L. Q. Chen, Electrochim. Acta, 2012, 81, 155–160.

50 J. Wang, J. L. Liu, D. L. Chao, J. X. Yan, J. Y. Lin and Z. X. Shen, Adv. Mater., 2014, 26, 7162–7169.

Nanoscale Accepted Manuscript